

Feature-Rich Electronic Properties of Sliding Bilayer Germanene

Hsin-Yi Liu and Jhao-Ying Wu*

Cite This: *ACS Omega* 2022, 7, 42304–42312

Read Online

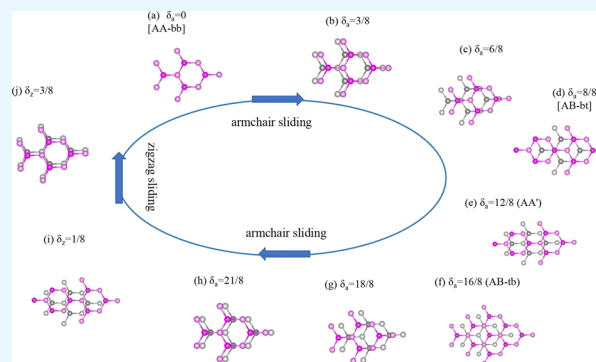
ACCESS |

Metrics & More

Article Recommendations

Supporting Information

ABSTRACT: This study employs first-principles calculations to elucidate the properties of sliding bilayer germanene (BLGe). The buckled structure of germanene can afford a greater number of metastable stacking configurations than planar graphene and enrich the electronic properties. Herein, a detailed analysis of the structural variety, shift-dependent energy bands, and spatial charge densities of BLGe is presented. The projected density of states (PDOS) reveals diverse structures such as plateaus, dips, symmetric/asymmetric peaks, and shoulders. The low-lying ones of the prominent structures could correspond to single or multiorbital hybridization, depending on the stacking configuration.



INTRODUCTION

Graphene, the first material composed of an atomically thin film, possesses unique electronic, optical, thermal, and mechanical properties.¹ Its outstanding performance has prompted the development of several two-dimensional (2D) materials in the last few years. These materials include phosphorene,^{2,3} arsenene,^{4–6} transition metal dichalcogenides (e.g., MoS₂, GaSe, WSe₂, WTe₂),^{7,8} organic crystals,⁹ and artificial 2D lattices.^{10,11} Among these materials, the 2D hexagonal structures formed by Si and Ge, namely, silicene and germanene,^{12–14} are the most similar to graphene. However, in contrast to the planar configuration of graphene, silicene and germanene exhibit low-buckled structures that are more thermally stable than their planar counterparts^{12,15,16} (except that some conditions could lead to quantum phase transitions¹⁷). Because of these buckled structures and the greater atomic numbers of Ge and Si than that of C, silicene and germanene have stronger spin–orbit interactions (SOIs). Theoretical calculations predict that the SOIs induce 1.55 and 23.9 meV band gaps in silicene and germanene, respectively.^{18–22} SOIs play a key role in the observation of the quantum spin Hall effect (QSHE) at moderate temperatures,^{23–25} and the buckling structure is useful in tuning the band gap via an externally applied electrical field. These two features, which are crucial for the development of field-effect devices, are more prominent in germanene than in silicene. Further, the carrier mobility of germanene is predicted to be 2–3 times that of silicene, owing to the greater buckling and the weaker coupling of charge carriers with in-plane phonons.²² Therefore, germanene is a potentially better candidate than silicene for the development of electronic devices. The functionalized germanenes also attract much interest due to their wide applications in various fields

including supercapacitors, photocatalysts, and anodes in Li-ion batteries. For example, germanene and methyl germanene can be easily synthesized via topotactical deintercalation of the layered Zintl phase calcium germanide (CaGe₂) with aqueous acid or methyl halide, respectively.^{26,27}

The electronic properties of 2D materials are sensitive to lattice symmetry. Layer stacking is a practical method of breaking this symmetry. For instance, AB- (also known as Bernal) and AA-stacked bilayer graphenes (BLGs) exhibit parabolic and linear low-energy bands, respectively.^{28,29} Further, covalent bonding between two monolayer silicene/germanene sheets could lead to the integration of intrinsic magnetism and band gap opening.³⁰ Notably, sliding or twisting a bilayer system can afford multiple metastable stacking configurations.^{31–34} In the case of silicene and germanene, each layer can be divided into top and bottom sublattices owing to the buckling characteristic, leading to several stacking patterns that cannot be attained using planar BLGs. A thorough study of the sliding process can offer a comprehensive understanding of the stacking-enriched geometric and electric properties. Importantly, germanene has a greater buckling height than graphene and silicene. Therefore, exceptionally shift-dependent properties are expected in germanene.

In this study, density functional theory (DFT), implemented using the Vienna Ab initio Simulation Package (VASP), is used

Received: August 14, 2022

Accepted: October 31, 2022

Published: November 9, 2022



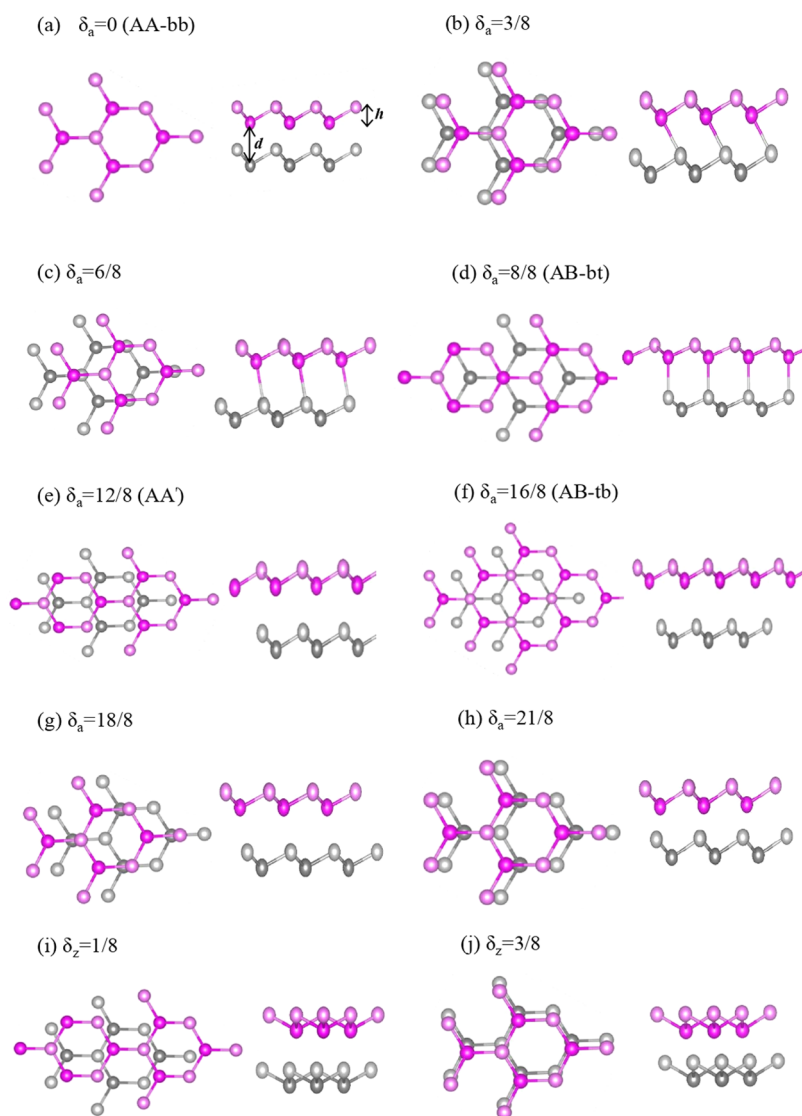


Figure 1. Top (left panels) and side (right panels) views of the geometric structures of BLGes with the relative shifts along the armchair (a–h) and zigzag (i, j) directions.

to examine sliding bilayer germanene (BLGe). Specifically, the geometric structures, energy bands, spatial charge densities, and orbital-decomposed density of states are studied. The interlayer–atomic interactions, depending on the stacking order, result in the different degrees of low-lying band mixings, the energy splitting/degeneracy between highly symmetric points, and the different numbers of middle-energy saddle points, oscillating parabolic subbands, partially flat bands, band anticrossings, and constant-energy loops. They are associated with the number, intensity, and divergent forms of van Hove singularities (vHs) in the density of states (DOS). For example, the saddle points, band anticrossings, and partially flat bands can result in logarithmically symmetric DOS peaks. These prominent vHs, close to or at the Fermi level, might cause diverse optical/magneto-optical spectra, unusual quantum Hall conductivities, and various single- and many-particle Coulomb excitations at low frequencies. Further, the magnified low-lying DOS could generate new phases of matter with desirable properties, such as superconductivity and density waves.³⁵ These interesting phenomena hardly occur in monolayer germanene due to the monotonic V-shape DOS

around $E_F = 0$. The large variety and tunability of these vHs mean that it is possible to engineer the abovementioned physical properties as well as their related applications in quantum transport, thermoelectric effects, nanolasing, biosensing, etc. The theoretically predicted geometric structures, valence bands, and density of states could be further validated by high-resolution measurements using scanning tunneling microscopy/tunneling electron microscopy (STM/TEM^{36,37}), angle-resolved photoemission spectroscopy (ARPES³⁸), and scanning tunneling spectroscopy (STS),³⁹ respectively.

■ GEOMETRIC STRUCTURES

Each bilayer stacking configuration contains four germanium atoms in a unit cell. The two sublattices A and B in each layer are equivalent on the (x, y) plane. The sliding BLGe is created by a relative shift δ_a (along the armchair direction) or δ_z (along the zigzag direction) between the two layers. In our calculations, the shift distance δ_a or δ_z is fixed, but the z positions of all atoms are relaxed. Further, δ_a and δ_z are in units of their periodic lengths, $3b$ and $\sqrt{3}b$, respectively, where b is the bond length. Notably, the periodic length of the shift

Table 1. Geometric Properties of Sliding Bilayer Germanene: Lattice Constant, Interlayer Distances d , Ge–Ge Bond Lengths b , and Ground-State Energies E_0 Per Unit Cell and Per Atom^a

	lattice	E_0	E_0	b	d	h
	constant (Å)	(eV/unit cell)	(eV/atom)	(Å)	(Å)	(Å)
monolayer germanene	4.06	−8.02	−4.01	2.44		0.69
$\delta_a = 0$ (AA-bb)	3.955	−17.34	−4.33	2.53	2.955	1.12
$\delta_a = 3/8$	4.01	−17.40	−4.35	2.518	2.547	0.95
$\delta_a = 6/8$	4.012	−17.33	−4.33	2.456	2.585	0.80
$\delta_a = 8/8$ (AB-bt)	4.011	−17.31	−4.33	2.442	2.598	0.78
$\delta_a = 12/8$ (AA')	3.992	−17.23	−4.31	2.458	2.627	0.86
$\delta_a = 16/8$ (AB-tb)	3.996	−16.96	−4.24	2.428	4.129	0.77
$\delta_a = 18/8$	3.989	−16.99	−4.25	2.46	3.63	0.85
$\delta_a = 21/8$	3.993	−17.35	−4.34	2.512	2.736	1.05
$\delta_z = 1/8$	3.998	−17.26	−4.31	2.469	2.619	0.88
$\delta_z = 3/8$	3.983	−17.37	−4.34	2.519	2.681	1.06

^aBuckling heights h are also shown.

distance δ_a of sliding BLGe is twice that of sliding BLG owing to the buckled structure. The several δ_a and δ_z values chosen in this study are shown in Figure 1. Specifically, $\delta_a = 0$ denotes the highly symmetric AA-bb stack (Figure 1a). The upper layer of this stack was shifted along the x direction (the armchair direction), as shown in Figure 1b–h. Subsequently, the highly symmetric stacking configurations owing to the shift included AB-bt ($\delta_a = 8/8$ in Figure 1d), AA ($\delta_a = 12/8$ in Figure 1e), and AB-tb ($\delta_a = 16/8$ in Figure 1f), where “b” represents the bottom and “t” corresponds to the top atoms in each sublayer. Lastly, Figure 1i,j shows configurations for which $\delta_z = 1/8$ and $3/8$, respectively, along the y direction (the zigzag direction), from $\delta_a = 12/8$.

The geometric parameters of various monolayer and bilayer germanenes are shown in Table 1. The latter exhibits a much lower ground-state energy E_0 than that of the former owing to the considerable attractive forces between the two sublayers. The lowest E_0 occurs in the configuration with $\delta_a = 3/8$, suggesting that this is the most stable geometric structure. In general, the interlayer distance d of the BLGes is shorter than that of BLG³³ (except that of AB-tb BLGe) because of the buckling. The buckling height h in the BLGes ranges from 0.77 to 1.22 Å, which is greater than that in monolayer germanene, 0.69 Å. The increased h is expected to produce more prominent multiorbital hybridizations of Ge-(4s, 4p_x, 4p_y, 4p_z) and considerably affect the fundamental properties.

RESULTS AND DISCUSSION

Energy Bands. The low-lying valence and conduction bands of monolayer germanene are characterized by a pair of linear bands dominated by the π bonding of the 4p_z orbital around the Fermi level at the K point (Figure 2a). These bands are generally symmetric about $E_F = 0$, with a narrow gap of approximately 23.9 meV caused by the SOIs. The π band initiates at the valley between the Γ and M points and exhibits a Γ valley at −0.55 eV and a saddle M (M') point at −1.15 eV. The M and M' points are degenerate owing to the sixfold rotational symmetry. These saddle points accumulate several electronic states and exhibit prominent optical absorption peaks. They are observed in various carbon-related sp²-bonding systems, such as layered graphenes,^{40–45} carbon nanotubes,^{46–48} and graphite.^{49–54} The σ band, created by the 4s, 4p_x, and 4p_y orbitals, initiates at the K valley and shows a saddle M point at −2 eV. The final valence valley is located at the Γ point at −0.4 eV, higher than the saddle M point of the π

band. This is in contrast to the cases of graphene and silicene. The SOI creates π and σ band anticrossings at the Γ valley and in the Γ – M path. The deep s band, which terminates at the Γ point at $E^v = -0.35$ eV, slightly overlaps with the σ band. The above features illustrate the weak band mixings and the clear $\pi/\sigma/s$ bandwidth in monolayer germanene.

The band structures are remarkably diversified by layer stacking. The electronic structure of AA-bb ($\delta_a = 0$) entails six valence and four conduction bands, which is double the number of valence and conduction bands in monolayer germanene, as shown in Figure 2b. The lowest conduction band exceeds E_F and reaches $E = -0.45$ eV at the M (M') point. Notably, this generates numerous free holes, and thus, the system is metallic. Further, the weak energy dispersion around the band-edge state creates constant-energy loops, which might result in a prominent Van Hove singularity (presented later in Figure 4). Furthermore, the interlayer interactions considerably decrease and increase the π valence and conduction band energies, respectively, at the K point compared to those of monolayer germanene. However, the highest-valence saddle M (M') point among those of the BLGes, at $E^v \approx -0.9$ eV, is higher than that of monolayer germanene, which is at $E^v \approx -1.15$ eV. In the range of $E^{sv} = -3$ – -1 eV, there are many band anticrossings due to the SOIs and the π and σ band mixings. In other words, the composite valley structures of the π and σ bands in monolayer germanene (Figure 2a) along $\Gamma \rightarrow M \rightarrow K$ and $K \rightarrow M \rightarrow \Gamma$, respectively, cannot survive in this bilayer system. Further, the energy of the final s band valley at the Γ point increases, while that of the initial valleys of the π and σ bands, between the Γ and M points and at the K point, respectively, decreases. This causes a 0.6 (1.8) eV overlap between the s and π (σ) bands. In short, the interlayer interactions increase the band mixings and overlaps, making it difficult to determine the bandwidths of the π , σ , and s bands.

The electronic energy spectrum is sensitive to the relative shift between the two layers. As δ_a increases from 0 to $3/8$, the sixfold rotational symmetry becomes twofold symmetry, resulting in energy splitting (at approximately 0.5 eV) between the M and M' points, as shown in Figure 2c. This causes strong anisotropic energy dispersions along $K \rightarrow M \rightarrow \Gamma$ and $K \rightarrow M' \rightarrow \Gamma$. The saddle-point structures only survive at the M point. The lowest conduction and highest valence bands exceed E_F in the Γ – M path and at the Γ point, respectively. Consequently, these bands afford fewer free carriers than those in the $\delta_a = 0$

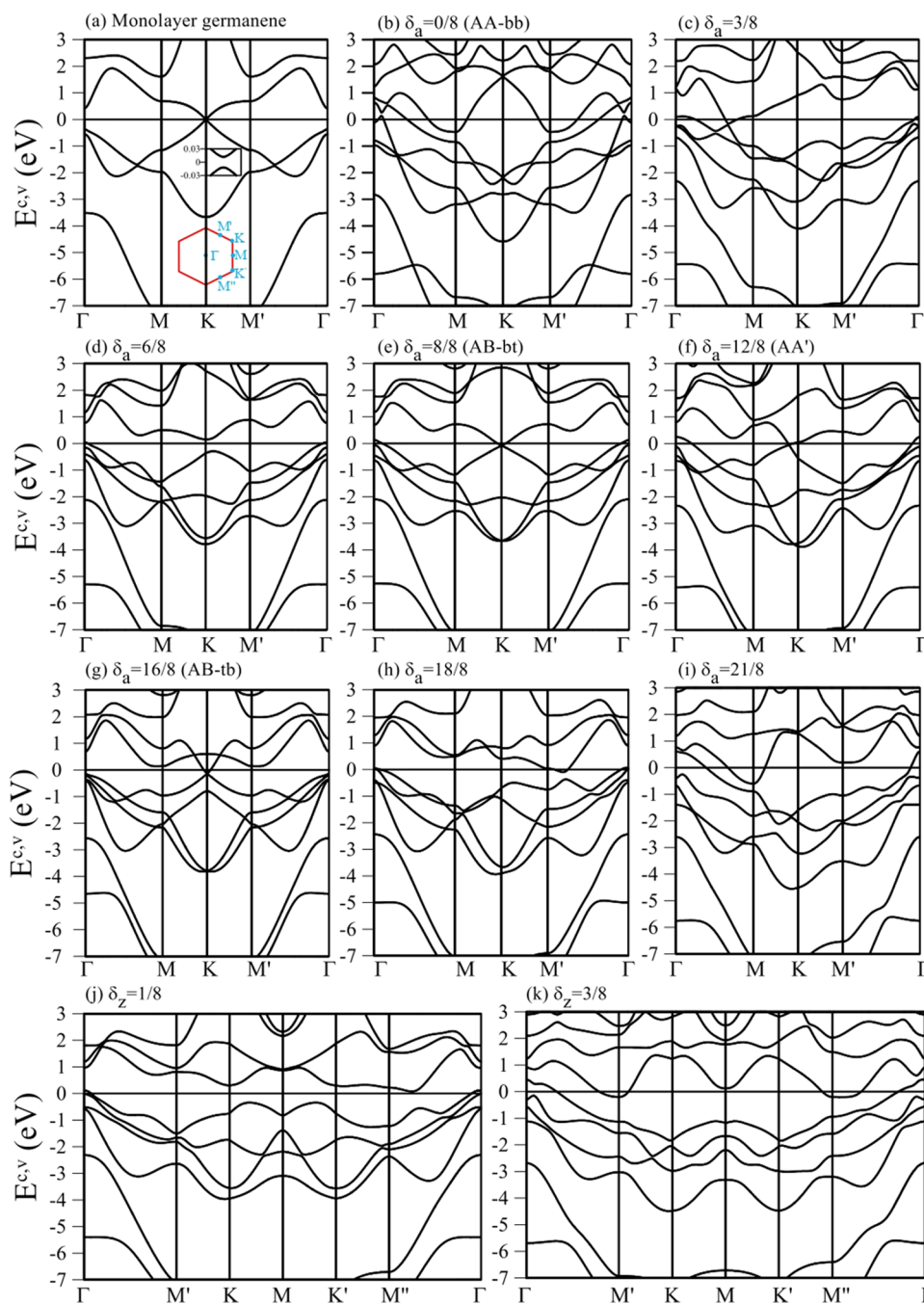


Figure 2. 2D band structures for monolayer germanene in (a) and BLGes with the relative shifts along the armchair (b–i) and zigzag (j, k) directions. The first Brillouin zone with highly symmetric points is illustrated in (a). Also, the inset in (a) demonstrates a gap of approximately 23.9 meV.

configuration (Figure 2b). Therefore, this system is similar to a semimetal. The highest and second highest valence bands exhibit many band-edge states, including valleys, partially flat bands, and constant-energy loops, owing to their frequent anticrossings. The small anticrossings along $K \rightarrow M \rightarrow \Gamma$ are caused by the SOIs, whereas the large ones along $K \rightarrow M' \rightarrow \Gamma$ are mainly induced by the π and σ band mixings. This anisotropy could impart interesting physical properties, such as polarization-dependent optical selection rules.⁵⁵ With a further shift to $\delta_a = 6/8$ (Figure 2d), a pair of oscillating parabolic subbands, mostly contributed by the π electrons, surround $E_F = 0$. They create the constant-energy loops near the K point and the two linear bands intersecting at $E_F = 0$ along $K \rightarrow \Gamma$

(shown in Figure S1a of the Supporting Information). The few existing free carriers are induced by the valence σ parabolic valley touching E_F at the Γ point. Therefore, the system is similar to a zero-gap semiconductor.

At $\delta_a = 8/8$, the bilayer yields the highly symmetric AB-bt stack with sixfold rotational symmetry, as demonstrated by the degenerate M and M' points (Figure 2e). Two π -bands intersect at the K point near $E_F = 0$. They are roughly linearly dispersive along $K \rightarrow M$ (M'), similar to those in monolayer germanene, but are parabolic and exhibit a tiny overlap near E_F along $K \rightarrow \Gamma$ (shown in Figure S1b in the Supporting Information). The cone structure arising from the π -electrons suggests that the low-energy physical properties, e.g., the

magnetic quantization⁵⁶ and magneto-optical selection rules,⁵⁷ of this configuration could be simulated using the phenomenological model. From $\delta_a = 8/8$ to $12/8$ (AA' stack in Figure 2f), the degeneracy of M and M' points is destroyed, and the pair of linear bands moves toward the M point. The small band overlap along $K \rightarrow \Gamma$ is replaced by the highly asymmetric parabolic dispersions against $E_F = 0$. Furthermore, the σ parabolic valley creates an increased number of free electrons at the Γ point.

Another highly symmetric stack, AB-tb, is obtained when $\delta_a = 16/8$ (Figure 2g). This system has the longest interlayer distance and the shortest buckling height (Table 1). Notably, the vdWs force plays an important role in stabilizing this structure and has a substantial impact on energy dispersions. The low-lying bands around the K point are characterized by a pair of parabolic valleys with zero energy spacing between them. These parabolic valleys belong to the oscillating parabolic subbands along $K \rightarrow M$ (M') $\rightarrow \Gamma$. Similar to the case of $\delta_a = 8/8$ (AB-bt), the two parabolic valleys have a tiny overlap along $K \rightarrow \Gamma$ (Figure S1c in the Supporting Information). Because of the weak interlayer coupling, the other valence bands distant from $E_F = 0$ behave similarly to those of monolayer germanene. That is, the π and σ bands exhibit composite valley structures along $\Gamma \rightarrow M \rightarrow K$ and $\rightarrow M \rightarrow \Gamma$, respectively, with very tiny band anticrossings.

The low-lying paired parabolic bands in AB-tb are destroyed completely with a slight shift to $\delta_a = 18/8$ (Figure 2h). This is owing to the breaking of the sixfold rotation symmetry and the enhanced π and σ band mixings. With a further shift to $\delta_a = 21/8$ (Figure 2i), numerous free holes and electrons appear at the M and Γ points, respectively. Further, the energy of the initial parabolic K valley is lowered, causing more overlapping with the s bands. The band anticrossings along $K \rightarrow M \rightarrow \Gamma$ are enlarged and are relatively similar to those in the case of $\delta_a = 0$ ($\delta_a = 24/8$). Nevertheless, the energy splitting between the M and M' points remains prominent, illustrating the sensitivity of the highly symmetric points to the shift.

Sliding an AA' stack ($\delta_a = 12/8$) in the zigzag direction results in the initial AA-bb stack ($\delta_a = 0$). In this process, the band anticrossings along all paths are enlarged, increasing the number of parabolic valleys and constant-energy loops, as shown in Figure 2j,k for $\delta_z = 1/8$ and $3/8$, respectively. Further, additional energy splitting is generated between the M' and M'' points owing to the breaking of mirror symmetry about the dimer lines. The lowest conduction band-edge states are moved from the K to the M' (M'') points when δ_z increases; furthermore, a few saddle M' (M'') points are gradually formed in the middle-energy region. Consequently, the system transforms from a semimetal-like one ($\delta_z = 1/8$) to a metal-like one ($\delta_z = 3/8$).

Spatial Charge Density. Spatial charge distributions can be employed to identify and examine single- and multiorbital hybridizations due to various chemical bondings.^{58–60} Monolayer germanene possesses σ (the red part) and π (the green part) bondings between neighboring atoms, as shown in Figure 3a. In planar graphene, the red part is almost a rectangle, indicating the strong directionality of the σ bonding and the orthogonality between the σ and π bondings. However, in germanene, the red part is similar to a dumbbell, indicating a small degree of nonorthogonality between the σ and π bondings due to the buckled structure. The non-orthogonality could be further enhanced by the interlayer interactions.

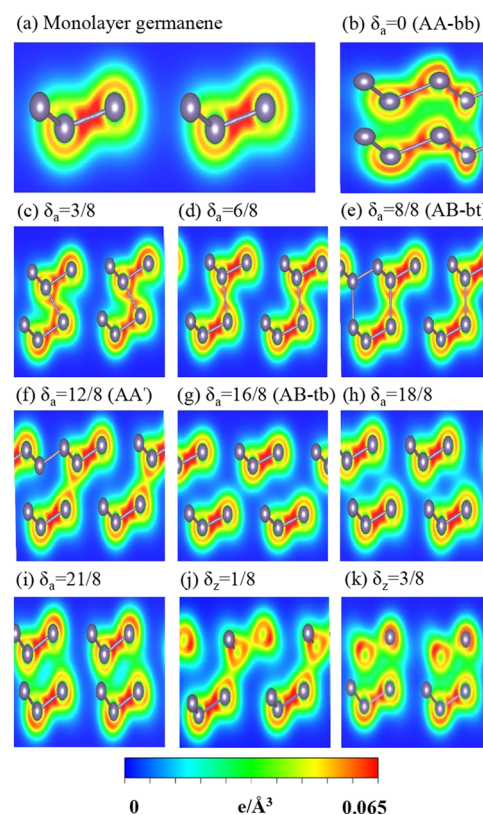


Figure 3. Spatial charge densities on the (x, z) -plane for monolayer germanene in (a) and BLGs with the relative shifts along the armchair (b–i) and zigzag (j, k) directions.

The exceptional variation in the spatial charge density distributions owing to the interlayer interactions is shown in Figure 3b–k. The charge densities are transferred from each monolayer to the interlayer spacing, forming π , σ , or sp^3 bondings, depending on the stacking configuration. The weak and low-directional interlayer π -bondings (the green part), similar to those in the cases with $\delta_a = 0$, $21/8$ and $\delta_z = 3/8$, afford several free carriers, and thus, the systems are metals. The opposite is true for σ or sp^3 interlayer bondings (the red and yellow parts), such as those in the cases with $\delta_a = 3/8$ – $12/8$ and $\delta_z = 1/8$, wherein the systems exhibit semimetallic features. In some cases, such as for $\delta_a = 16/8$ and $18/8$, the charge density between two layers is small, and the interlayer coupling mainly relies on the vdWs force. The interlayer sp^3 bonding (the yellow part) gradually weakens upon shifting from $\delta_a = 12/8$ (Figure 3f) to $\delta_z = 1/8$ (Figure 3j) and $3/8$ (Figure 3k) and is replaced by π -bonding, changing the system from semimetallic to metallic.

Density of States. The projected density of states (PDOS) reveals the contributions of the $4s$, $4p_x$, $4p_y$, and $4p_z$ orbitals and is useful in distinguishing various orbital hybridizations. Special structures in energy bands, such as the extreme states of parabolic dispersions, saddle points, and constant-energy loops, shown in Figure 2, can result in prominent shoulders, logarithmically symmetric peaks, and asymmetric structures in the square-root form, respectively, as shown in Figure 4. For monolayer germanene (Figure 4a), the DOSs reveal a linear energy dependence that is asymmetric about $E_F = 0$, corresponding to a modified Dirac cone. The shoulder structure at -0.5 eV is related to the parabolic valley of the σ band at the Γ point, and the symmetric peak at -1.1 eV is

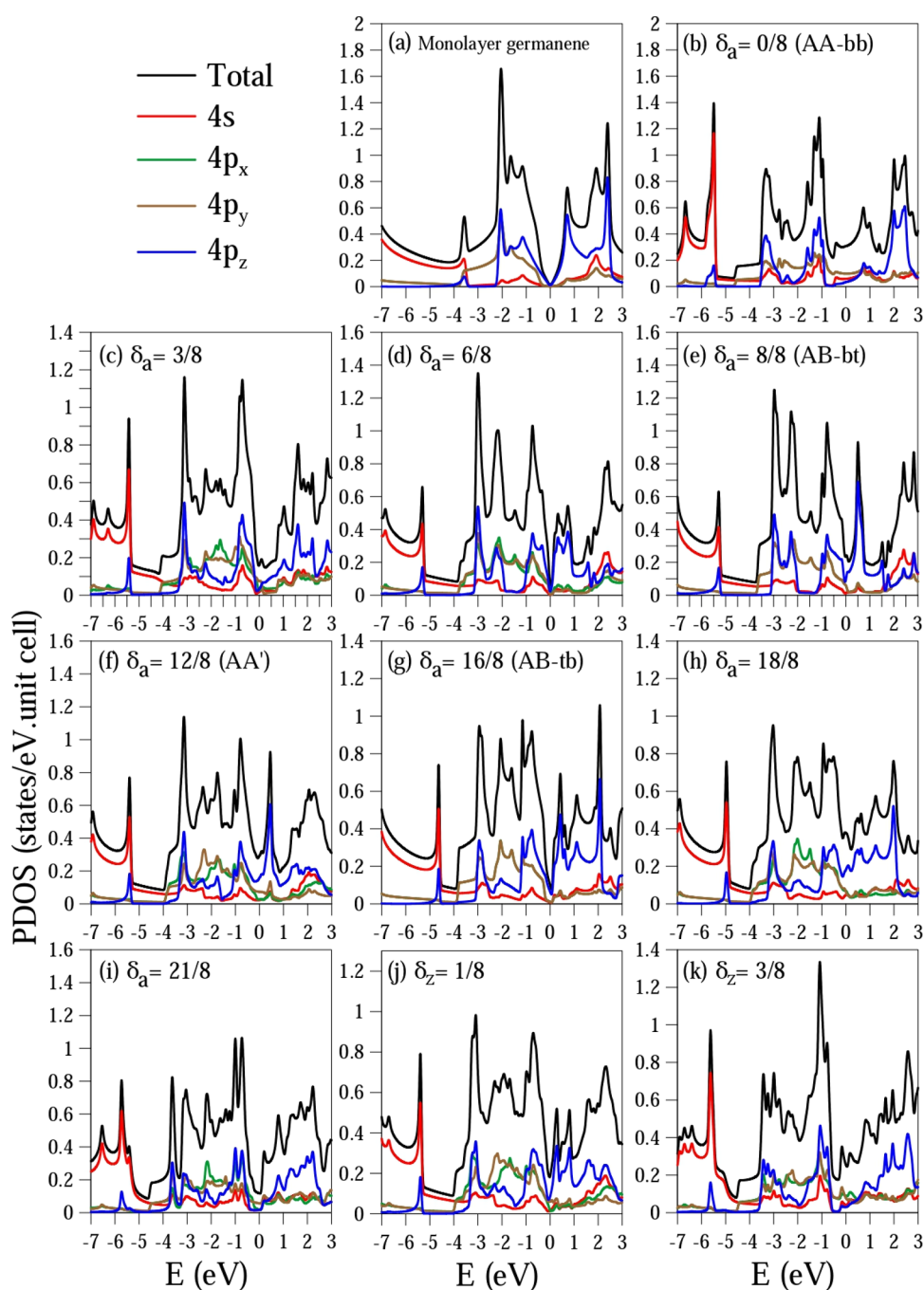


Figure 4. Orbital-projected densities of states for monolayer germanene in (a) and BLGs with the relative shifts along the armchair (b–i) and zigzag (j, k) directions.

associated with the saddle M point of the π band. The energy of the shoulder structure is greater than that of the symmetric peak, and this scenario is opposite to that in monolayer graphene and silicene,³⁴ wherein the $3p_x$ and $3p_y$ orbitals are negligible over the symmetric peak. The other symmetric peak at -1.6 eV is caused by the anticrossing between the π and σ bands, while the peak at -2 eV is associated with the saddle M point of the σ band. All orbitals exhibit a peak at the latter position, and among them, the $4p_x$, $4p_y$, and $4p_z$ orbitals have comparable peak intensities. In the -3.5 eV $< E < -2.3$ eV region, the contributions of the $4s$ and $4p_z$ orbitals almost vanish. The peak at $E = -3.5$ eV denotes the overlap between the σ and s bands. Beyond this peak, the $4s$ orbital becomes

dominant. Thus, it was possible to characterize the initial, middle, and final energies of the π , σ , and s bands.

The interlayer interactions complicate the DOSs, as shown in Figure 4b–k. The semimetallic and metallic properties of the various configurations are reflected in the DOS values at E_F . Weakly dispersive energy bands that exceed E_F can impart a high DOS (>0.2) and metallicity, such as in the cases with $\delta_a = 0, 8/8, 12/8$, and $18/8$ and $\delta_z = 3/8$. For $\delta_a = 6/8, 16/8$, and $\delta_z = 1/8$, the DOSs exhibit asymmetric V shapes around $E_F = 0$, corresponding to modified linear bands or a pair of parabolic valleys. Such systems are categorized as semimetals. In these systems, the low-energy DOSs (in the range of $|E^{(v)}| < 0.5$ eV) are mainly dominated by $4p_z$ orbitals. In general, it is difficult

to distinguish the initial, middle, and final π and σ bands because all $4s$, $4p_x$, $4p_y$, and $4p_z$ orbitals have considerable contributions for $E > -3$ eV in all stacking configurations. Furthermore, the newly created saddle M (M') points, energy splitting between highly symmetric points, oscillating parabolic subbands, and frequent band anticrossings can result in several symmetric and asymmetric peaks. Specifically, many stacking configurations possess up to two symmetric peaks with prominent sp^3 hybridization at $E = -1$ to -0.8 eV, e.g., $\delta_a = 3/8$, $6/8$, $8/8$, $12/8$, and $21/8$ and $\delta_z = 3/8$. Such peaks correspond to the saddle M (M') points, band anticrossings, and partially flat bands. STS measurements may be used to examine the abovementioned structures in the DOSs and to distinguish the effect of the π and sp^3 bondings on the low- and middle-energy physical properties.

CONCLUSIONS

The fundamental properties of sliding BLGs were explored using first-principles calculations. Stacking-dependent interlayer interactions, including π , σ , sp^3 bondings, and the vdWs force, diversified the electronic properties. The feature-rich energy bands exhibited low-lying band mixings, energy splitting/degeneracy between highly symmetric points, several middle-energy saddle points, oscillating parabolic subbands, partially flat bands, many band anticrossings, and constant-energy loops. This induced multiple symmetric/asymmetric peaks in the PDOS, corresponding to various degrees of orbital hybridizations. Compared to sliding bilayer silicene, sliding BLGs has a greater buckling height and stronger interlayer coupling, which enhances the band mixings and creates more partially flat bands and anticrossings, leading to more low-lying logarithmically symmetric peaks in the DOS. Further, the energy dispersion, free-carrier density, and energy splitting/degeneracy between the highly symmetric points are more sensitive to the stacking order, e.g., bt or tb stack. Hence, the shift distance considered in this work is twice larger than that in the previous study on sliding bilayer silicene.³⁴ The larger shift distance affords a larger variety of electronic properties and van Hove singularities. In the future, STS measurements may be used to examine the number of middle-energy symmetric peaks and to verify the degeneracy, splitting, or destruction of saddle M and M' points. These results are useful in understanding the properties of BLGs with subangstrom misalignments that may occur by design or unintentionally in experiments.^{61–63} Further, a sliding bilayer system is helpful to understand/explain the complicated electronic properties of a twisted bilayer system due to their similar stacking orders in certain regions.⁶⁴ Especially, the more prominent buckled structure and the stronger interlayer coupling of germanene than those of graphene and silicene could allow a larger rotation angle and further diversify/complicate the electronic properties.

METHODS

First-principles calculations based on DFT were performed using VASP.⁶⁵ The projector-augmented wave approach (PAW; pseudopotentials in refs 66, 67) was employed to characterize the electron-ion crystal potential. Electron–electron interactions were evaluated using an exchange–correlation functional based on Perdew–Burke–Ernzerhof (PBE) generalized gradient approximation.⁶⁸ The cutoff energy of the Bloch wave functions, which were built from

complete plane waves, was set to 500 eV. A sufficiently large vacuum layer (20 Å) was added to replicate systems along the perpendicular direction and to avoid artificial interactions between neighboring supercells. Furthermore, Grimme's semiempirical DFT-D2 correction was adopted to calculate the van der Waals (vdWs) interactions.⁶⁹ All atomic coordinates were relaxed until the Hellmann–Feynman force was less than 0.01 eV/Å, along with a total energy difference of $\Delta E < 10^{-5}$ eV. For specific calculations of optimal geometric structures and electronic properties, the first Brillouin zones were sampled using $100 \times 100 \times 1$ k -points via the γ scheme. The orbital-projected DOS calculation was performed with $150 \times 150 \times 1$ k -points. Finally, spin–orbital coupling (SOC) configurations were included in the VASP calculations of the total ground-state energies.⁷⁰

ASSOCIATED CONTENT

Supporting Information

The Supporting Information is available free of charge at <https://pubs.acs.org/doi/10.1021/acsomega.2c05219>.

Energy spectra of $\delta_a = 6/8$, $8/8$, and $16/8$ along the $\Gamma \rightarrow M \rightarrow K \rightarrow \Gamma$ direction (PDF)

AUTHOR INFORMATION

Corresponding Author

Jhao-Ying Wu – Center of General Studies, National Kaohsiung University of Science and Technology, Kaohsiung 811213, Taiwan; Department of Energy and Refrigerating Air-Conditioning Engineering, National Kaohsiung University of Science and Technology, Kaohsiung 811213, Taiwan; orcid.org/0000-0001-5563-5167; Email: yarst5@nkust.edu.tw

Author

Hsin-Yi Liu – Department of Physics/QTC/Hi-GEM, National Cheng Kung University, Tainan 70148, Taiwan

Complete contact information is available at: <https://pubs.acs.org/doi/10.1021/acsomega.2c05219>

Notes

The authors declare no competing financial interest.

ACKNOWLEDGMENTS

This work was supported by the National Science Council of Taiwan (Grant Nos. 107-2112-M-194-010-MY3 and MOST 110-2112-M-992-001).

REFERENCES

- (1) Neto, A. H. C.; Guinea, F.; Peres, N. M. R.; Novoselov, K. S.; Geim, A. K. The electronic properties of graphene. *Rev. Mod. Phys.* **2009**, *81*, 109–162.
- (2) Akhtar, M.; Anderson, G.; Zhao, R.; Alruqi, A.; Mroczkowska, J. E.; Sumanasekera, G.; Jasinski, J. B. Recent advances in synthesis, properties, and applications of phosphorene. *npj 2D Mater. Appl.* **2017**, *1*, No. 5.
- (3) Woomey, A. H.; Farnsworth, T. W.; Hu, J.; Wells, R. A.; Donley, C. L.; Warren, S. C. Phosphorene: Synthesis, Scale-Up, and Quantitative Optical Spectroscopy. *ACS Nano* **2015**, *9*, 8869–8884.
- (4) Kong, N.; Zhang, H.; Feng, C.; Liu, C.; Xiao, Y.; Zhang, X.; Mei, L.; Kim, J. S.; Tao, W.; Ji, X. Arsenene-mediated multiple independently targeted reactive oxygen species burst for cancer therapy. *Nat. Commun.* **2021**, *12*, No. 4777.

- (5) Shah, J.; Wang, W.; Sohail, H. M.; Uhrberg, R. I. G. Experimental evidence of monolayer arsenene: an exotic 2D semiconducting material. *2D Mater.* **2020**, *7*, No. 025013.
- (6) Bhuvanewari, R.; Nagarajan, V.; Chandiramouli, R. Recent advances in arsenene nanostructures towards prediction, properties, synthesis and applications. *Surf. Interfaces* **2022**, *28*, No. 101610.
- (7) Lv, R.; Robinson, J. A.; Schaak, R. E.; Sun, D.; Sun, Y.; Mallouk, T. E.; Terrones, M. Transition Metal Dichalcogenides and Beyond: Synthesis, Properties, and Applications of Single- and Few-Layer Nanosheets. *Acc. Chem. Res.* **2015**, *48*, 56–64.
- (8) Hoang, A. T.; Qu, K.; Chen, X.; Ahn, J.-H. Large-area synthesis of transition metal dichalcogenides via CVD and solution-based approaches and their device applications. *Nanoscale* **2021**, *13*, 615–633.
- (9) Zhang, L.; Hasan, M. M.; Tang, Y.; Khan, A. R.; Yan, H.; Yildirim, T.; Sun, X.; Zhang, J.; Zhu, J.; Zhang, Y.; Lu, Y. 2D organic single crystals: Synthesis, novel physics, high-performance optoelectronic devices and integration. *Mater. Today* **2021**, *50*, 442–475.
- (10) Esposito, C.; Barros, M. R.; Hernández, A. D.; Carvacho, G.; Di Colandrea, F.; Barboza, R.; Cardano, F.; Spagnolo, N.; Marrucci, L.; Sciarrino, F. Quantum walks of two correlated photons in a 2D synthetic lattice. *npj Quantum Inf.* **2022**, *8*, No. 34.
- (11) Solomos, M. A.; Claire, F. J.; Kempa, T. J. 2D molecular crystal lattices: advances in their synthesis, characterization, and application. *J. Mater. Chem. A* **2019**, *7*, 23537–23562.
- (12) Cahangirov, S.; Topsakal, M.; Aktürk, E.; Şahin, H.; Ciraci, S. Two- and One-Dimensional Honeycomb Structures of Silicon and Germanium. *Phys. Rev. Lett.* **2009**, *102*, No. 236804.
- (13) Matthes, L.; Pulci, O.; Bechstedt, F. Massive Dirac quasiparticles in the optical absorbance of graphene, silicene, germanene, and tinene. *J. Phys.: Condens. Matter* **2013**, *25*, No. 395305.
- (14) Balendhran, S.; Walia, S.; Nili, H.; Sriram, S.; Bhaskaran, M. Elemental Analogues of Graphene: Silicene, Germanene, Stanene, and Phosphorene. *Small* **2015**, *11*, 640–652.
- (15) Takeda, K.; Shiraiishi, K. Theoretical possibility of stage corrugation in Si and Ge analogs of graphite. *Phys. Rev. B* **1994**, *50*, 14916–14922.
- (16) Guzmán-Verri, G. G.; Yan Voon, L. C. L. Electronic structure of silicon-based nanostructures. *Phys. Rev. B* **2007**, *76*, No. 075131.
- (17) Huang, C.; Zhou, J.; Wu, H.; Deng, K.; Jena, P.; Kan, E. Quantum Phase Transition in Germanene and Stanene Bilayer: From Normal Metal to Topological Insulator. *J. Phys. Chem. Lett.* **2016**, *7*, 1919–1924.
- (18) Boettger, J. C.; Trickey, S. B. First-principles calculation of the spin-orbit splitting in graphene. *Phys. Rev. B* **2007**, *75*, No. 121402.
- (19) Gmitra, M.; Konschuh, S.; Ertler, C.; Ambrosch-Draxl, C.; Fabian, J. Band-structure topologies of graphene: Spin-orbit coupling effects from first principles. *Phys. Rev. B* **2009**, *80*, No. 235431.
- (20) Abdelouahed, S.; Ernst, A.; Henk, J.; Maznichenko, I. V.; Mertig, I. Spin-split electronic states in graphene: Effects due to lattice deformation, Rashba effect, and adatoms by first principles. *Phys. Rev. B* **2010**, *82*, No. 125424.
- (21) Liu, C.-C.; Feng, W.; Yao, Y. Quantum Spin Hall Effect in Silicene and Two-Dimensional Germanium. *Phys. Rev. Lett.* **2011**, *107*, No. 076802.
- (22) Ye, X.-S.; Shao, Z.-G.; Zhao, H.; Yang, L.; Wang, C.-L. Intrinsic carrier mobility of germanene is larger than graphene's: first-principle calculations. *RSC Adv.* **2014**, *4*, 21216–21220.
- (23) Katsuragawa, N.; Nishizawa, M.; Nakamura, T.; Inoue, T.; Pakdel, S.; Maruyama, S.; Katsumoto, S.; Palacios, J. J.; Haruyama, J. Room-temperature quantum spin Hall phase in laser-patterned few-layer 1T-MoS₂. *Commun. Mater.* **2020**, *1*, No. 51.
- (24) Haruyama, J. Quantum-spin-Hall phases and 2D topological insulating states in atomically thin layers. *J. Appl. Phys.* **2021**, *129*, No. 090902.
- (25) Popescu, A.; Rodriguez-Lopez, P.; Woods, L. M. Composition and stacking dependent topology in bilayers from the graphene family. *Phys. Rev. Mater.* **2019**, *3*, No. 064002.
- (26) Chia, H. L.; Sturla, J.; Webster, R. D.; Pumera, M. Functionalized 2D Germanene and Silicene Enzymatic System. *Adv. Funct. Mater.* **2021**, *31*, No. 2011125.
- (27) Ng, S.; Sturla, J.; Vyskocil, J.; Lazar, P.; Martincova, J.; Plutnar, J.; Pumera, M. Two-Dimensional Functionalized Germanenes as Photoelectrocatalysts. *ACS Nano* **2021**, *15*, 11681–11693.
- (28) McCann, E.; Koshino, M. The electronic properties of bilayer graphene. *Rep. Prog. Phys.* **2013**, *76*, No. 056503.
- (29) Liu, Z.; Suenaga, K.; Harris, P. J. F.; Iijima, S. Open and Closed Edges of Graphene Layers. *Phys. Rev. Lett.* **2009**, *102*, No. 015501.
- (30) Wang, X.; Wu, Z. Intrinsic magnetism and spontaneous band gap opening in bilayer silicene and germanene. *Phys. Chem. Chem. Phys.* **2017**, *19*, 2148–2152.
- (31) Andrei, E. Y.; MacDonald, A. H. Graphene bilayers with a twist. *Nat. Mater.* **2020**, *19*, 1265–1275.
- (32) Tao, S.; Zhang, X.; Zhu, J.; He, P.; Yang, S. A.; Lu, Y.; Wei, S.-H. Designing Ultra-flat Bands in Twisted Bilayer Materials at Large Twist Angles: Theory and Application to Two-Dimensional Indium Selenide. *J. Am. Chem. Soc.* **2022**, *144*, 3949–3956.
- (33) Tran, N. T. T.; Lin, S.-Y.; Glukhova, O. E.; Lin, M.-F. Configuration-Induced Rich Electronic Properties of Bilayer Graphene. *J. Phys. Chem. C* **2015**, *119*, 10623–10630.
- (34) Liu, H.-y.; Lin, S.-Y.; Wu, J.-y. Stacking-configuration-enriched essential properties of bilayer graphenes and silicenes. *J. Chem. Phys.* **2020**, *153*, No. 154707.
- (35) Li, Z.; Zhuang, J.; Chen, L.; Ni, Z.; Liu, C.; Wang, L.; Xu, X.; Wang, J.; Pi, X.; Wang, X.; Du, Y.; Wu, K.; Dou, S. X. Observation of van Hove Singularities in Twisted Silicene Multilayers. *ACS Cent. Sci.* **2016**, *2*, 517–521.
- (36) Zhang, K.; Bernard, R.; Borensztein, Y.; Cruguel, H.; Prévot, G. Growth of germanium-silver surface alloys followed by in situ scanning tunneling microscopy: Absence of germanene formation. *Phys. Rev. B* **2020**, *102*, 125418.
- (37) Borysiuk, J.; Bożek, R.; Strupiński, W.; Wyszomolek, A.; Grodecki, K.; Stępniewski, R.; Baranowski, J. M. Transmission electron microscopy and scanning tunneling microscopy investigations of graphene on 4H-SiC(0001). *J. Appl. Phys.* **2009**, *105*, No. 023503.
- (38) Kubo, O.; Kinoshita, S.; Sato, H.; Miyamoto, K.; Sugahara, R.; Endo, S.; Tabata, H.; Okuda, T.; Katayama, M. Kagome-like structure of germanene on Al(111). *Phys. Rev. B* **2021**, *104*, No. 085404.
- (39) Walhout, C. J.; Acun, A.; Zhang, L.; Ezawa, M.; Zandvliet, H. J. W. Scanning tunneling spectroscopy study of the Dirac spectrum of germanene. *J. Phys.: Condens. Matter* **2016**, *28*, No. 284006.
- (40) Lin, C. Y.; Wu, J. Y.; Ou, Y. J.; Chiu, Y. H.; Chiu, Y. H.; Lin, M. F. Magneto-electronic properties of multilayer graphenes. *Phys. Chem. Chem. Phys.* **2015**, *17*, 26008–26035.
- (41) Do, T. N.; Shih, P. H.; Chang, C. P.; Lin, C. Y.; Lin, M. F. Rich magneto-absorption spectra in AAB-stacked trilayer graphene. *Phys. Chem. Chem. Phys.* **2016**, *18*, 17597–17605.
- (42) Koshino, M. Stacking-dependent optical absorption in multilayer graphene. *New J. Phys.* **2013**, *15*, No. 015010.
- (43) Chiu, C. W.; Chen, R. B. Influence of electric fields on absorption spectra of AAB-stacked trilayer graphene. *Appl. Phys. Express* **2016**, *9*, No. 065103.
- (44) Chen, S. C.; Chiu, C. W.; Wu, C. L.; Lin, M. F. Shift-enriched optical properties in bilayer graphene. *RSC Adv.* **2014**, *4*, 63779–63783.
- (45) Chiu, C. W.; Huang, Y. C.; Shyu, F. L.; Lin, M. F. Excitation spectra of ABC-stacked graphene superlattice. *Appl. Phys. Lett.* **2011**, *98*, No. 261920.
- (46) Shyu, F. L.; Lin, M. F. Electronic and optical properties of narrow-gap carbon nanotubes. *J. Phys. Soc. Jpn.* **2002**, *71*, 1820–1823.
- (47) Lin, M. F.; Shung, K. W. K. Plasmons and optical properties of carbon nanotubes. *Phys. Rev. B* **1994**, *50*, 17744–17747.
- (48) Ruzicka, B.; Degiorgi, L.; Gaal, R.; Thien-Nga, L.; Bacsá, R.; Salvatá, J. P.; Forro, L. Optical and dc conductivity study of potassium-doped single-walled carbon nanotube films. *Phys. Rev. B* **2000**, *61*, R2468–R2471.

- (49) Djurišić, A. B.; Li, E. H. Optical properties of graphite. *J. Appl. Phys.* **1999**, *85*, 7404–7410.
- (50) Chiu, C. W.; Lee, S. H.; Chen, S. C.; Shyu, F. L.; Lin, M. F. Absorption spectra of AA-stacked graphite. *New J. Phys.* **2010**, *12*, No. 083060.
- (51) Taft, E. A.; Philipp, H. R. Optical Properties of Graphite. *Phys. Rev.* **1965**, *138*, A197–A202.
- (52) Ichikawa, Y. H.; Kobayashi, K. Optical properties of graphite in the infrared region. *Carbon* **1966**, *3*, 401–406.
- (53) Dovbeshko, G. I.; Romanyuk, V. R.; Pidgirnyi, D. V.; Cherepanov, V. V.; Andreev, E. O.; Svirko, Y. P.; et al. Optical Properties of Pyrolytic Carbon Films Versus Graphite and Graphene. *Nanoscale Res. Lett.* **2015**, *10*, No. 234.
- (54) Ergun, S.; Yasinsky, J. B.; Townsend, J. R. Transverse and longitudinal optical properties of graphite. *Carbon* **1967**, *5*, 403–408.
- (55) Wang, Y.; Yu, G.; Rösner, M.; Katsnelson, M. I.; Lin, H.-Q.; Yuan, S. Polarization-Dependent Selection Rules and Optical Spectrum Atlas of Twisted Bilayer Graphene Quantum Dots. *Phys. Rev. X* **2022**, *12*, No. 021055.
- (56) Do, T. N.; Shih, P. H.; Gumbs, G.; Huang, D.; Chiu, C. W.; Lin, M. F. Diverse magnetic quantization in bilayer silicene. *Phys. Rev. B* **2018**, *97*, No. 125416.
- (57) Do, T. N.; Gumbs, G.; Shih, P. H.; Huang, D.; Chiu, C. W.; Chen, C. Y.; Lin, M. F. Peculiar optical properties of bilayer silicene under the influence of external electric and magnetic fields. *Sci. Rep.* **2019**, *9*, No. 36547.
- (58) Bena, C.; Montambaux, G. Remarks on the tight-binding model of graphene. *New J. Phys.* **2009**, *11*, No. 095003.
- (59) Nguyen, D. K.; Lin, Y. T.; Lin, S. Y.; Chiu, Y. H.; Trana, N. T. T.; Lin, M. F. Fluorination-enriched electronic and magnetic properties in graphene nanoribbons. *Phys. Chem. Chem. Phys.* **2017**, *19*, 20667–20676.
- (60) Lin, S. Y.; Lin, Y. T.; Tran, N. T. T.; Su, W. P.; Lin, M. F. Feature-rich electronic properties of aluminum-adsorbed graphenes. *Carbon* **2017**, *120*, 209–218.
- (61) Feng, X.; Kwon, S.; Park, J. Y.; Salmeron, M. Superlubric Sliding of Graphene Nanoflakes on Graphene. *ACS Nano* **2013**, *7*, 1718–1724.
- (62) Liu, Z.; Yang, J.; Grey, F.; Liu, J. Z.; Liu, Y.; Wang, Y.; Yang, Y.; Cheng, Y.; Zheng, Q. Observation of Microscale Superlubricity in Graphite. *Phys. Rev. Lett.* **2012**, *108*, No. 205503.
- (63) Choi, S.-M.; Jhi, S.-H.; Son, Y.-W. Anomalous Optical Phonon Splittings in Sliding Bilayer Graphene. *ACS Nano* **2013**, *7*, 7151–7156.
- (64) Wu, J. B.; Zhang, X.; Tan, P. H.; Feng, Z. H.; Li, J. Electronic structure of twisted bilayer graphene. *Acta Phys. Sin.* **2013**, *62*, No. 157302.
- (65) Kresse, G.; Furthmüller, J. Efficient iterative schemes for ab initio total-energy calculations using a plane-wave basis set. *Phys. Rev. B* **1996**, *54*, No. 11169.
- (66) Blöchl, P. E. Projector augmented-wave method. *Phys. Rev. B* **1994**, *50*, 17953–17979.
- (67) Kresse, G.; Joubert, D. From ultrasoft pseudopotentials to the projector augmented-wave method. *Phys. Rev. B* **1999**, *59*, 1758–1775.
- (68) Perdew, J. P.; Burke, K.; Ernzerhof, M. Generalized Gradient Approximation Made Simple. *Phys. Rev. Lett.* **1996**, *77*, 3865–3868.
- (69) Grimme, S. Semiempirical GGA-type density functional constructed with a long-range dispersion correction. *J. Comput. Chem.* **2006**, *27*, 1787–1799.
- (70) Steiner, S.; Khmelevskiy, S.; Marsmann, M.; Kresse, G. Calculation of the magnetic anisotropy with projected-augmented-wave methodology and the case study of disordered Fe_{1-x}Co_x alloys. *Phys. Rev. B* **2016**, *93*, No. 224425.